



PET/MR of pediatric bone tumors: what the radiologist needs to know

Jennifer Padwal¹ · Lucia Baratto¹ · Amit Chakraborty² · Kristina Hawk¹ · Sheri Spunt⁴ · Raffi Avedian⁵ · Heike E. Daldrup-Link^{1,3,4}

Received: 27 February 2022 / Revised: 11 June 2022 / Accepted: 29 June 2022
© The Author(s), under exclusive licence to International Skeletal Society (ISS) 2022

Abstract

Integrated 2-deoxy-2-[fluorine-18]fluoro-D-glucose (¹⁸F-FDG) positron emission tomography (PET)/magnetic resonance (MR) imaging can provide “one stop” local tumor and whole-body staging in one session, thereby streamlining imaging evaluations and avoiding duplicate anesthesia in young children. ¹⁸F-FDG PET/MR scans have the benefit of lower radiation, superior soft tissue contrast, and increased patient convenience compared to ¹⁸F-FDG PET/computerized tomography scans. This article reviews the ¹⁸F-FDG PET/MR imaging technique, reporting requirements, and imaging characteristics of the most common pediatric bone tumors, including osteosarcoma, Ewing sarcoma, primary bone lymphoma, bone and bone marrow metastases, and Langerhans cell histiocytosis.

Keywords Bone sarcoma · Pediatric cancer · PET/MR · Positron emission tomography · Magnetic resonance

Introduction

Integrated MRI and ¹⁸F-FDG-PET provide efficient staging of children (ages 2–12 years of age) and adolescents (ages 12–21 years of age) with malignant bone tumors by evaluating the primary tumor and the whole body in one session [1]. Although radiography is important for initial evaluation, MR has become the mainstay for locoregional staging and surgical planning of pediatric bone tumors. By adding metabolic information, ¹⁸F-FDG-PET can be used for detection of metastases throughout the body. The integration of MRI and ¹⁸F-FDG-PET can streamline the staging

examination by acquiring local and whole-body staging in a single session.

¹⁸F-FDG-PET/MR has similar diagnostic accuracy compared to ¹⁸F-FDG-PET/CT for lesion detection, with overall highly correlative standardized uptake value (SUV) measurements despite differences in attenuation correction methods (albeit relatively decreased bone marrow SUV in ¹⁸F-FDG-PET/MR compared to ¹⁸F-FDG-PET/CT) [2–4]. Advantages of integrated ¹⁸F-FDG-PET/MR over ¹⁸F-FDG-PET/CT include at least 73% reduced radiation exposure for the patient, superior soft tissue contrast, and increased patient convenience as patients undergo one imaging test and one anesthesia (rather than two imaging tests and applications of anesthesia required for MRI and ¹⁸F-FDG-PET/CT) [2]. This article summarizes important aspects of ¹⁸F-FDG-PET/MR that a radiologist needs to know about malignant bone tumors in pediatric patients including imaging techniques, reporting requirements, and the typical imaging appearance of common pediatric bone tumors. Important imaging features will be emphasized including joint infiltration, tumor thrombus, lymph node metastases, and bone/bone marrow metastases, which impact the patient’s prognosis and help plan appropriate local and systemic therapy.

✉ Heike E. Daldrup-Link
H.E.Daldrup-Link@stanford.edu

¹ Department of Radiology, Stanford University, Stanford, CA 94305, USA

² Department of Radiology, Massachusetts General Hospital, Boston, MA 02114, USA

³ Cancer Imaging Program, Stanford Cancer Institute, Stanford, USA

⁴ Department of Pediatrics, Stanford University, 725 Welch Rd., Rm. 1665, Stanford, CA 94305-5614, USA

⁵ Department of Surgery, Division of Pediatric Orthopedic Surgery, Lucile Packard Children’s Hospital, Stanford University, Stanford, CA 94305, USA

Imaging technique

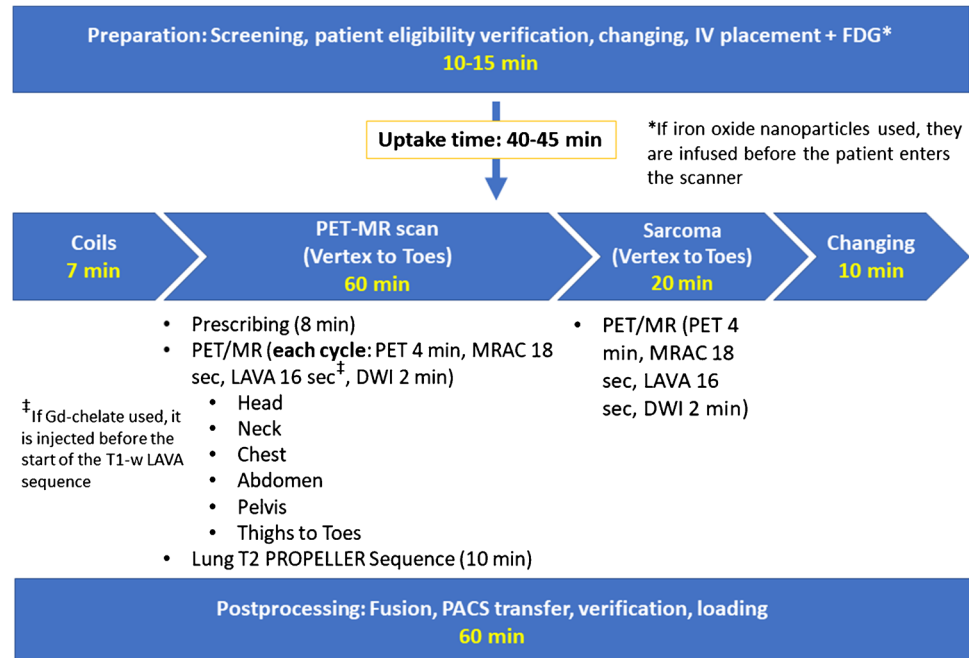
Appropriate staging of malignant bone tumors includes a radiograph, a local MRI for evaluation of the primary tumor extent (especially if a surgery or biopsy is planned), and a head-to-toe scan to evaluate for multifocal disease or metastases. Common protocol concepts for ¹⁸F-FDG-PET/MR scans at our and other institutions includes acquisition of whole-body PET scans with pediatric-tailored ¹⁸F-FDG doses, a whole-body MRI scan and a local MRI scan in the same session. However, MRI pulse sequence protocols and parameters vary widely between different centers [5]. In our experience, pediatric patients typically tolerate an exam time of 1 h or less. We split the 1-h exam time between 30 min for a whole-body scan and 30 min for a local tumor scan. We start with the 30-min whole-body scan to provide us with an overview of multifocal disease and give us the ability to prescribe dedicated sequences to one or more areas. Multiple injection protocols for integrated ¹⁸F-FDG-PET/MR have been proposed. Some investigators obtain unenhanced MRI scans and fuse these with ¹⁸F-FDG-PET scans. To enable strong vascular and tissue enhancement throughout the entire scan, we either obtain a Gd-chelate enhanced whole body MRI scan and fuse it with a sequential ¹⁸F-FDG-PET scan, similar to the approach for a contrast-enhanced PET/CT, or alternatively, we administer iron oxide nanoparticles intravenously at 1–2 h before the scan and then obtain truly simultaneous whole body MRI and ¹⁸F-FDG-PET scans. Iron oxide nanoparticles have been employed as a promising alternative to gadolinium-based

contrast agents given their biocompatibility and favorable magnetic properties, in addition to their biodegradability and nontoxic nature [6–8]. At our institution, iron oxide nanoparticles helped us to address logistical and diagnostic challenges, such as improving time-limited vessel and tissue enhancement for integrated local and whole-body scans and detecting bone marrow lesions in highly cellular hematopoietic marrow of children and adolescents. Alternatively, Gd chelates can be administered. In the setting of Gd-chelate use, multiple contrast injection schemes have been proposed: (1) whole-body ¹⁸F-FDG-PET, followed by a contrast-enhanced whole body MRI scan, followed by local scan in the delayed post-contrast phase, or (2) whole-body ¹⁸F-FDG-PET, followed by a contrast-enhanced whole-body MRI scan and local scan with 50% dose injections for either exam. At our institution, we inject ¹⁸F-FDG at a dose of 3 Mbq/kg at 45 min before start of the exam. This accounts for an additional 15 min to place the patient in the PET/MR scanner, so that PET scans start at 60 min after radiotracer injection. An example of the ¹⁸F-FDG-PET MR imaging workflow is provided in Fig. 1.

Whole-body staging

In order to co-localize ¹⁸F-FDG-PET and MRI data, multiple strategies exist, whereby the ¹⁸F-FDG-PET data can be co-localized with unenhanced, Gd-enhanced, or Fe-enhanced whole-body MRI scans [9–11]. Additionally, depending on the region of interest, some centers perform a local MRI scan prior to or after the whole-body scan [11, 12]. In our experience, we found axial, contrast-enhanced breath-hold

Fig. 1 Example of the ¹⁸F-FDG-PET/MR imaging workflow



gradient echo (GE) sequences with simultaneously acquired ^{18}F -FDG-PET data to be the most time efficient, which can be acquired within 20–30 min [13]. Of note, we acquire non-breathhold Dixon sequences for attenuation correction of ^{18}F -FDG-PET data and additional “high resolution” breath hold GE sequences for anatomical co-registration of PET data [14]. In the future, these can likely be combined into one single sequence. We generate maximum intensity projections (MIP) of the ^{18}F -FDG-PET data to provide an overview of the presence and location of metastases throughout the body. We also generate coronal and/or sagittal reconstructions of the fused ^{18}F -FDG PET/MR scans.

We add a dedicated sequence with radial k-space filling (PROPELLER technique: Periodically Rotated Overlapping Parallel Lines with Enhanced Reconstruction) or ultrashort TE T2-weighted sequence of the chest to evaluate for pulmonary nodules. These sequences can assess for pulmonary nodules with higher accuracy compared to traditionally used T2-weighted fat-saturated sequences [15]. To date, our patients still need an additional chest CT for the detection of pulmonary nodules.

Primary tumor imaging

Next, it is important to obtain one coronal or sagittal T1-weighted non-fat-saturated fast spin echo sequence of the entire bone that involves the primary tumor, from upper to lower joint. This helps orthopedic surgeons measure the distance of a bone resection from the upper or lower joint surface and to plan for adequate positioning and length of a prosthesis. We obtain non-fat-saturated T1-weighted MR images before Gd-chelate injection, followed by fat-saturated T1-weighted MR images after Gd-chelate injection.

Then, it is important to apply a small field of view for a dedicated MR of the primary tumor with a surface coil, which includes a fat-saturated T2-weighted sequence in two planes (typically axial and coronal/sagittal), and a fat-saturated contrast-enhanced T1-weighted fast spin echo sequence in one or two planes, to delineate vascular/necrotic tumor areas and the presence of tumor thrombus.

Table 1 Imaging characteristics to include in radiology report

Primary tumor location (which bone, where in the bone, extraosseous soft tissue)
Primary tumor size in three dimensions
Cortical destruction
Pathological fracture
Joint involvement
Tumor infiltration of which extra-osseous compartments
Relation to neurovascular bundle (important: encasement can mean amputation)
Tumor thrombus
Skip lesions (focal lesion in same bone as the primary tumor)
Number, location, and size of metastases (different bone/tissue than primary tumor)
SUVmax of primary tumor and representative metastases
SUV mean of the liver and mediastinal blood pool (as a reference standard)

Radiology report

The radiology report of a bone tumor ^{18}F -FDG-PET/MR scan should include the typical imaging characteristics of the primary tumor as listed in Table 1. The primary tumor is measured in three dimensions. For osteosarcomas and Ewing sarcomas, for example, the tumor volume is calculated according to a tumor-type specific formula, where the 3D measurement based on the tumor length in x -, y -, and z -axis is multiplied by a factor F based on shape ($F = \pi/6$ or 0.524 for spherical versus $F = \pi/4$ or 0.785 for cylindrical tumors) [16]. A sample radiology report for a ^{18}F -FDG-PET/MR scan is included in Table 2.

Metastases are reported with regard to their location and number. On the ^{18}F -FDG PET scan, up to five target lesions are measured per patient, usually choosing the largest and “hottest” lesions. A lymph node with a short-axis measurement of less than 1 cm is typically defined as normal. In children, however, lymph nodes at the mandibular angles and in the inguinal regions can be slightly larger. Abnormal lymph nodes in children have a diameter of more than 1.5 cm and demonstrate ^{18}F -FDG-PET radiotracer signal greater than that of liver as an internal reference standard. If at all possible, we try to schedule the whole-body PET/MR exam before the initial biopsy of the primary tumor. After the biopsy, local lymph nodes are often positive on the ^{18}F -FDG-PET scan and can cause diagnostic difficulties. Metastases in lymph nodes and visceral organs are measured in three dimensions, in order to define their largest diameter.

It is important to describe the number, location, and size of pulmonary nodules in detail, as these are often resected. This includes careful description of pulmonary nodules which involve the hila or the pleura as this might make a lesion unresectable and can have implications on overall prognosis. For bone marrow metastases, it is important to describe if there is an extraosseous soft tissue component (bone marrow lesions alone are usually not measured).

Table 2 Sample radiology report**WHOLE-BODY F18-FDG PET-MRI: [Order Date]****CLINICAL HISTORY:** [Patient Age, Patient Gender, history]**COMPARISON:** [Date]**PROCEDURE COMMENTS:****Tracer information:** [18F-FDG/Ga-68 Dotatate/18F-DOPA/11C-Methionine]**Measured (injected) dose:** [Value] mCi**Injection site:** [Right antecubital fossa/Left antecubital fossa/Right hand/Left hand/Right forearm/Left forearm/PICC line/Right wrist/Left wrist/Porta-A-Cath/Hickman/Right lower extremity/Left lower extremity]**Anatomical region:** [vertex to toes/anatomical regions]**IV contrast:** [Gadavist/Eovist/Multihance/Feraheme], [Value] mL**Sedation:** [None/Anesthesia]**Urinary Bladder Catheterization:** [None/Bladder catheter present]

Scan technique: Following IV administration of the radiopharmaceutical, images were acquired after an initial uptake phase using a 3 T PET-MRI scanner. Multiplanar, multisequence images of the total body were reviewed. For descriptive purposes, the maximum standard uptake value (SUV max) of metabolically active tissues is reported in g/mL, unless stated otherwise. For the purposes of this study MRI slice location are indicated on MRI series

Baseline measurements:**Mean mediastinal blood pool SUV**=[Value] g/mL**Mean liver SUV**=[Value] g/mL**FINDINGS:****-Index Lesions (SUVmax and three-dimensional measurements of the primary tumor and up to 5 additional lesions = 6 lesions total)**

1) Lesion description, measuring: [CT measurement, SUV: PET SUV, MR image: MR Table Position], previously: [previous measurements if available]

-Deauville Score (If applicable): [Score:1 (no uptake)/2 (uptake \leq mediastinum)/3 (uptake $>$ mediastinum $<$ liver)/4 (uptake $>$ liver)/5 (uptake $>$ liver or progressive disease)/X (uptake thought to be unrelated to lymphoma)]

-Ann Arbor Staging (if applicable): [Stage I/Stage II/Stage III/Stage IV]

IMPRESSION:

All other lesions including any measurable lesions over and above the 5 target lesions should be identified as non-target lesions and recorded at baseline. Measurements of these lesions are not required, but the presence, absence, or in rare cases unequivocal progression of each should be noted throughout follow-up. It is also important to describe metastases that involve nerves or other critical structures, which might require palliative radiation therapy.

For treatment monitoring, changes in size of the index lesions are described per organ system. Please note that Response Evaluation Criteria in Solid Tumors (RECIST) criteria do not apply to bone tumors [17]. This is because the soft tissue component typically shrinks in the axial plane while the longest longitudinal tumor extend in the bone typically changes only slightly after treatment. Therefore, measuring the longest tumor diameter in the bone only would underestimate therapy response of a bone tumor. However, soft tissue metastases are measured according to RECIST criteria, i.e., changes in the largest diameter (unidimensional measurement) of the metastases in the lungs and the short-axis diameter of the largest lymph node in the case of malignant lymph nodes (RECIST 1.1) [18].

The following sections will describe some of the most common pediatric bone tumors and their ^{18}F -FDG-PET/MR imaging characteristics.

Osteosarcoma

Osteosarcoma is the most common pediatric bone cancer, with approximately 75% occurring in patients ages 15–25 years (peaking in adolescence) and affecting 3–5/million males and 2–4/million females worldwide [19–21]. In 2021, the American Cancer Society estimated the incidence of new cases of bone and joint cancer to be 3,610 cases across the USA [22]. Primary tumors in long bones of the extremities have a relatively better prognosis than tumors in the central skeleton [23]. The American Cancer Society estimates the 5-year survival rate to be approximately 77% for localized disease, 27% in the presence of distant metastasis¹³, and 21% in case of local relapse [20]. Additionally, size of the primary tumor serves as another prognostic factor and is calculated by measuring tumor dimensions on MR images and using the formula for calculation of volume ($F \times AP \times RL \times SI = \text{volume}$), where F is

based on tumor shape ($F = \pi/6$ for ellipsoid tumors, $\pi/4$ for cylindrical tumors, and $\pi/5$ for all other tumor shapes) [24]. Tumor necrosis of $\geq 90\%$ after neoadjuvant chemotherapy is considered a good therapy response with a higher survival rate [20].

Osteosarcoma is a heterogenous disease with a wide spectrum of pathologic presentations and behavior [20, 25]. According to the World Health Organization (WHO), there are six subtypes, including high-grade central or conventional (most common), low-grade central, parosteal, periosteal, high-grade surface, and secondary [25, 26]. Conventional osteosarcoma typically appears as a destructive intramedullary mass in the metaphysis of long bones with new bone formation and aggressive periosteal reaction, often associated with hemorrhage and necrosis [21]. While soft tissue components of osteosarcoma are ^{18}F -FDG avid on PET scans, T2-hypointense bone forming components often have low ^{18}F -FDG avidity, leading to heterogenous appearance [20]. A photopenic center has been associated with poor prognosis. ^{18}F -FDG-PET can help distinguish between T2 signal associated with tumor tissue and peri-lesional edema. While tumor will be ^{18}F -FDG-PET avid, there should be no uptake associated with edema [27]. It is important to check for the presence of a tumor thrombus in adjacent veins, which has been described in up to 40% of osteosarcoma patients and need to be resected along with the tumor [28]. The three different subtypes of high-grade central osteosarcoma—osteoblastic, chondroblastic, and fibroblastic—can only be differentiated based on histology. Typically, a tumor will show varying degrees of each subtype with categorization based on the predominant cell type [21].

Telangiectatic osteosarcoma is an uncommon variant of high-grade osteosarcoma representing approximately 10% of all tumors [29]. Telangiectatic osteosarcoma appears as an aneurysmal lesion containing predominantly (90%) cystic and hemorrhagic components, with heterogenous signal on T1-weighted images and characteristic fluid–fluid levels on T2-weighted MRI scans (Fig. 2a–d). Distinction of telangiectatic osteosarcoma from aneurysmal bone cysts can be difficult. Nodular septal thickening and enhancement can be indicative of malignant tumor components [30]. Telangiectatic osteosarcoma appears diffusely heterogenous on ^{18}F -FDG-PET, with hypermetabolic solid tumor areas and photopenic necrosis/hemorrhage.

The most common surface osteosarcoma, the parosteal subtype, represents approximately 5% of all osteosarcomas [31, 32]. Parosteal osteosarcoma appears as a pedunculated and lobulated ossific density originating from the cortex, often with a cleavage plane separating the tumor and neighboring normal cortex. Typically, these are low-grade lesions arising most commonly from the metaphysis; however, parosteal osteosarcoma can demonstrate invasion into the medullary canal in both low- and high-grade cases, reaching

up to 50% in the latter [25]. The dense osteoid components of parosteal osteosarcomas are T1- and T2-hypointense while less mineralized components are T2-hyperintense. Parosteal osteosarcoma appears as a broad-based hypermetabolic mass on PET with possible medullary invasion but without periosteal new bone formation [33].

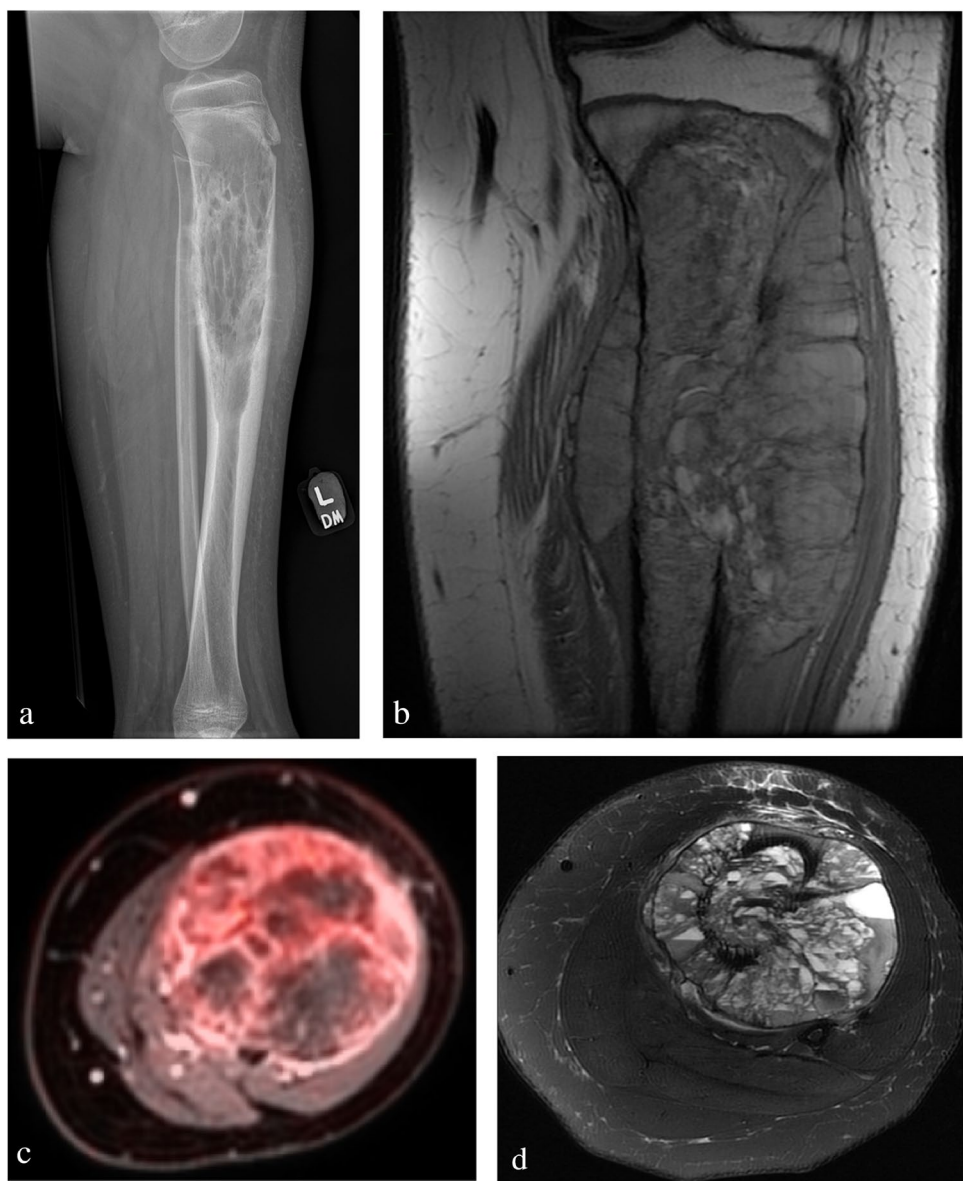
Periosteal osteosarcoma presents as a thickened scalloped cortex extending into a broad-based soft tissue mass with associated periosteal reaction [21]. These lesions typically affect the diaphysis and have a higher grade of anaplasia compared to parosteal osteosarcoma, but rarely invade the medullary canal. On MR, these lesions demonstrate heterogeneous iso- to hyperintensity on T2-weighted images with well-defined margins and possible calcified matrix which appears hypointense on all sequences (Fig. 3a–e) [32]. On ^{18}F -FDG-PET, periosteal osteosarcoma appears as a broad-based hypermetabolic soft tissue mass with cortical thickening, variable degree of periosteal reaction and rare medullary invasion (Fig. 3a–e) [33].

The primary method of surgical resection for osteosarcoma involves limb-preserving surgery with wide surgical margins whenever possible, with amputation indicated in cases of neurovascular invasion or extensive soft tissue involvement [34–37]. An important pre-operative imaging consideration in limb-preserving surgery is the presence of joint involvement by the tumor, which is the deciding factor between intra- versus extra-articular surgical approaches. The intra-articular approach is technically easier and has better post-operative functional outcomes for patients compared to the extra-articular approach. Joint extension in **osteosarcoma** suggests the tumor has spread to extrafascial spaces and is not restricted to anatomic barriers, necessitating extra-articular resection for local control.

A tumor thrombus can be seen in up to 40% of osteosarcomas and is typically discovered at baseline examination [38, 39]. Despite the high incidence of tumor thrombus in **osteosarcoma**, detection of tumor thrombi on preoperative imaging is often difficult given their small size [40, 41]. If the tumor thrombus is ^{18}F -FDG avid, then PET can be helpful to detect it, with SUVmax values ranging between 7.9 and 20 for tumor thrombi versus no increased SUVmax compared to mediastinal uptake for benign thrombi [42]. However, sub-centimeter tumor thrombi often show low ^{18}F -FDG uptake. The presence of intravascular tumor extension portends a poor prognosis, with average survival around 12–13 months [38]. In our experience, ^{18}F -FDG-PET/MR allows for more accurate assessment of the tumor thrombus burden and involved vasculature compared to ^{18}F -FDG-PET/CT due to the increased soft tissue contrast provided by MRI.

Skip lesions are a second, smaller focus of sarcoma in the same bone but anatomically distinct from the primary sarcoma, rarely seen in **osteosarcomas** and Ewing sarcomas (Fig. 4a–e) [43, 44]. Skip lesions are not considered

Fig. 2 Telangiectatic osteosarcoma of the left tibia in an 11-year-old male presenting with left leg pain and mass. **a** Lateral radiograph demonstrates an expansile mixed lucent and sclerotic lesion of the proximal left tibial metaphysis extending into the diaphysis. There is cortical destruction with sunburst type periosteal reaction and a partially calcified anterior soft tissue mass. **b** Sagittal T1-weighted MR image showing a heterogeneously hypointense expansile tumor of the proximal tibia with extensive cortical destruction and aggressive periosteal reaction. **c** PET/MR: Axial T1-weighted fat-suppressed image fused with ¹⁸F-FDG scan demonstrating heterogenous hypermetabolism of soft tissue components of the mass (SUV max 6.2). **d** Axial T2-weighted fat-suppressed MR image showing numerous fluid-fluid levels throughout the mass



metastases, but they can be associated with poor outcomes, with an average survival of 6 months to 2 years after diagnosis [45, 46]. Bone metastases, i.e., lesions in other bones, are uncommon in [osteosarcoma](#) at baseline and are typically late-term complications of advanced osteosarcoma [47]. The accuracy of detecting skip lesions and bone metastases, found in up to 25% of cases, was higher with ¹⁸F-FDG-PET than conventional imaging (95.2% versus 66.7%) [43]. MRI alone had an accuracy of 85.7% in young patients [48].

¹⁸F-FDG-PET was advantageous for the detection of lesions with a diameter of more than 1 cm in small bones, such as ribs and calvarium. MRI could better detect sub-centimeter lesions. Therefore, the two techniques have different blind spots and their combination leads to higher diagnostic accuracy than either technique alone [5]. ¹⁸F-FDG-PET also adds

value in detecting lymph node and visceral organ metastasis [20, 48].

The most common sites of metastasis for osteosarcoma include the lungs, bones, and rarely lymph nodes. To date, ¹⁸F-FDG-PET/MR can detect pulmonary nodules with a size down to 5 mm [41]. Further technical optimizations may enable detection of pulmonary nodules with a diameter of 3–5 mm. Lesions between 1 and 2 mm do not usually have therapeutic consequences.

Treatment for osteosarcoma includes induction chemotherapy followed by radical tumor resection. The patient only survives if the tumor can be completely excised with clear margins, including the biopsy tracts from the initial diagnosis. Following chemotherapy, osteosarcomas often only show a minor decline in tumor size. The gold standard

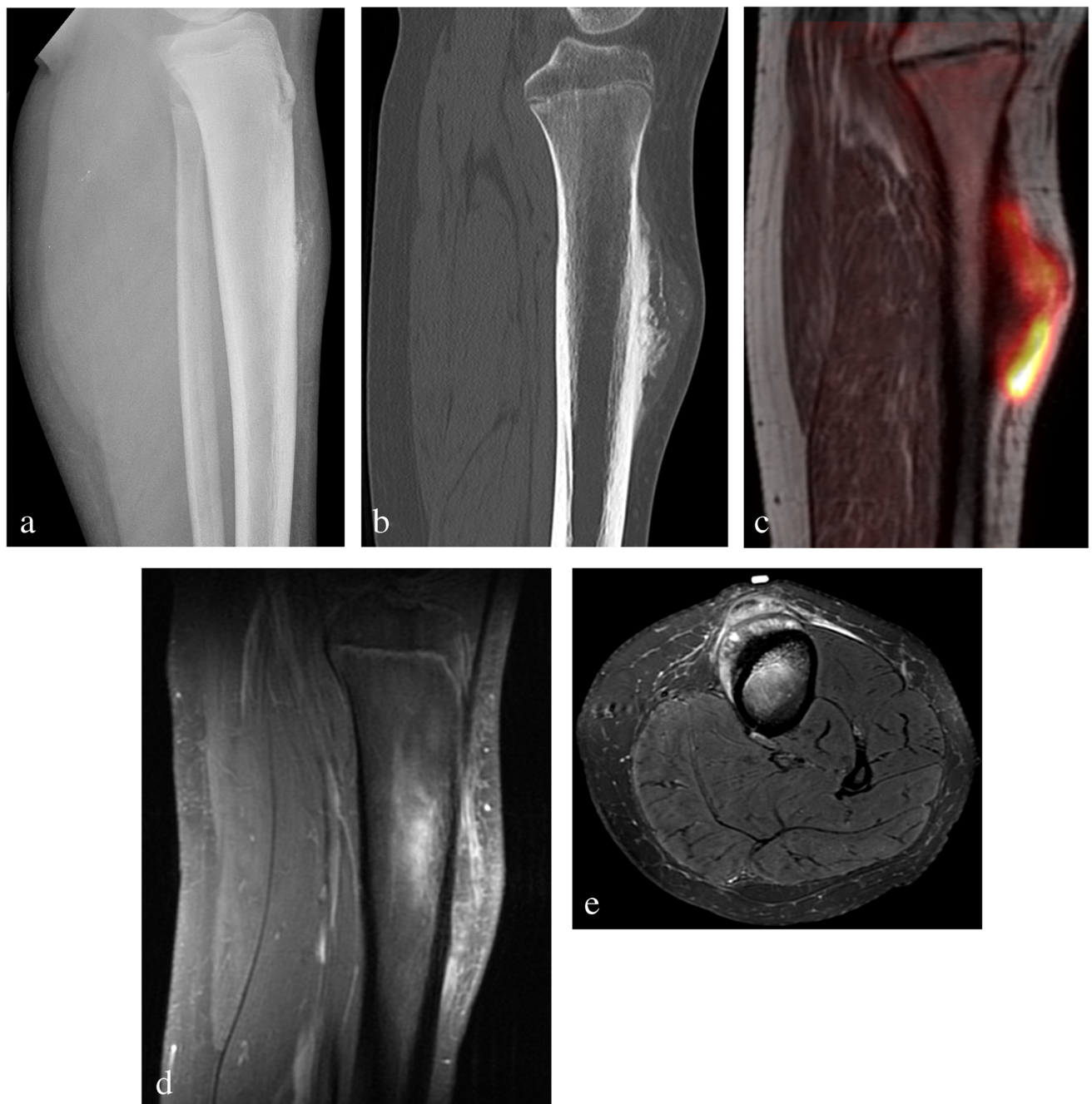


Fig. 3 Intermediate grade periosteal chondroblastic osteosarcoma of the left tibia in a 13-year-old female presenting with left lower extremity pain. **a** Lateral radiograph and **b** sagittal CT image of the left tibia/fibula showing a cortical based lesion involving the anterior proximal tibial diaphysis with aggressive periosteal bone formation and scalloping of the underlying cortex. **c** PET/MR sagittal T1-weighted fused image demonstrating a broad based, hypermetabolic soft tissue mass along the anterior proximal diaphysis of the left tibia (SUV max 12.6) with thickening of the underlying anterior cortex. **d** Sagittal T1-weighted fat-suppressed post contrast MR image and **e** axial PD-weighted fat-suppressed MR image showing heterogenous enhancement/hyperintensity of the anterior soft tissue component with small amount of medullary involvement posterior to the mass

bolic soft tissue mass along the anterior proximal diaphysis of the left tibia (SUV max 12.6) with thickening of the underlying anterior cortex. **d** Sagittal T1-weighted fat-suppressed post contrast MR image and **e** axial PD-weighted fat-suppressed MR image showing heterogenous enhancement/hyperintensity of the anterior soft tissue component with small amount of medullary involvement posterior to the mass

of response to chemotherapy is a histopathological diagnosis of 90% necrosis after tumor resection, which corresponds to good treatment response and was associated with better event-free survival and overall survival in [osteosarcoma](#)

patients by investigators at Memorial Sloan-Kettering Cancer Center [49–51]. Though histologic evaluation is still the gold standard, studies have shown that a decline in tumor SUV_{max} and metabolic rate of glucose consumption after

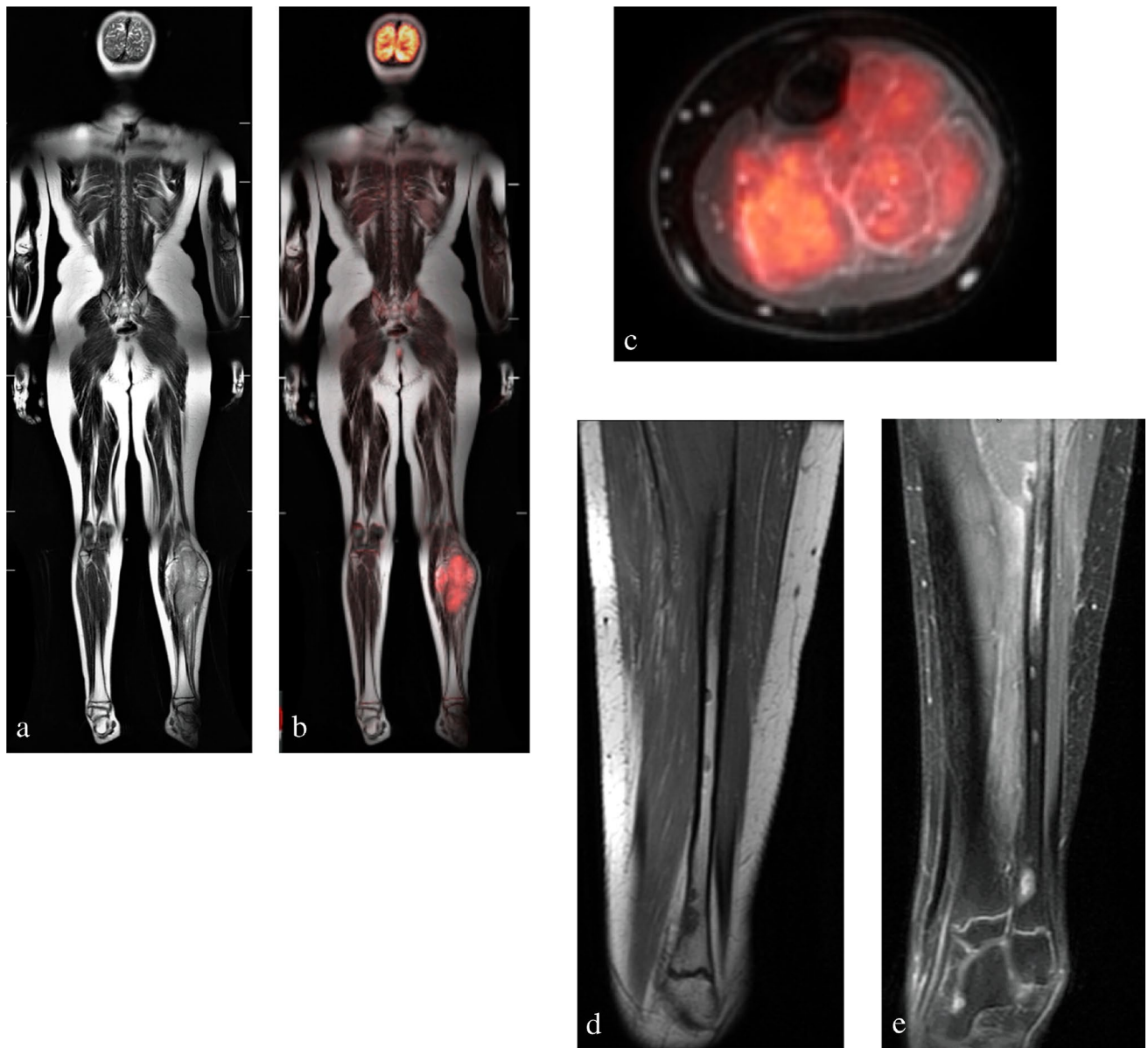


Fig. 4 Ewing sarcoma of the left fibula in a 10-year-old female patient presenting with a 3–4-month history of left foot drop, left lower extremity pain and paresthesias, and a large nontender mass in her left lower leg. **a** Coronal whole-body T2-weighted MR, **b** PET/MR: coronal T2-weighted MRI fused with ^{18}F -FDG PET, and **c** PET/MR: axial T1-weighted fat-suppressed postcontrast images. The ^{18}F -FDG PET/MRI scan shows a heterogenous T2-hyperin-

tense mass arising from the left proximal fibular diaphysis that demonstrates significant ^{18}F -FDG PET avidity (SUV_{\max} 5.6) and contrast enhancement on Gd-chelate enhanced T1-weighted MRI scans. **d** Sagittal T1-weighted MRI scan and **e** contrast-enhanced T1-weighted fat-suppressed MR image of the distal fibula showing discrete T1 hypointense lesions that enhance on postcontrast images, consistent with multiple intramedullary skip lesions

induction chemotherapy correlate well with tumor grade and predicted treatment response [20]. A post therapy SUV_{\max} of 5 was associated with poor response to therapy while a SUV_{\max} below 2.5 predicted a good response [52].

Finally, both ^{18}F -FDG-PET and MRI have been shown to accurately diagnose local recurrence with reported sensitivity of 88.2% for MRI and 73.7% for PET [20]. However, ^{18}F -FDG-PET can be helpful in distinguishing ^{18}F -FDG avid recurrence from

post-treatment fibrosis and in detecting recurrent tumor along metal prostheses which cause confounding artifacts on MRI.

Ewing sarcoma

Ewing sarcomas were reclassified in the 2020 WHO as part of the family of “Undifferentiated Small Round Cell Sarcomas of Bone and Soft Tissue” and are characterized by

EWSR1-ETS gene translocations [53–55]. Ewing sarcomas of the bones represent the second most common bone tumor in children [54]. Ewing sarcomas are aggressive cancers that typically arise from the bone marrow in the diaphysis of long bones in young children or from the bone marrow of the central skeleton in older children. Five-year overall survival rates for patients with localized disease are ~70–80% [54]. However, nearly a quarter of all patients present with treatment-resistant metastases at time of diagnosis and have 5-year survival rates of <30% [54, 56]. It is therefore very important for the radiologist to differentiate localized and metastasized tumors.

Extraskeletal and lower extremity Ewing sarcomas are associated with a better prognosis than tumors in the central skeleton [57]. In addition, a pathologic fracture at diagnosis, an age > 13 years, and a tumor length > 8 cm or a tumor volume > 200 ml are associated with a worse prognosis.

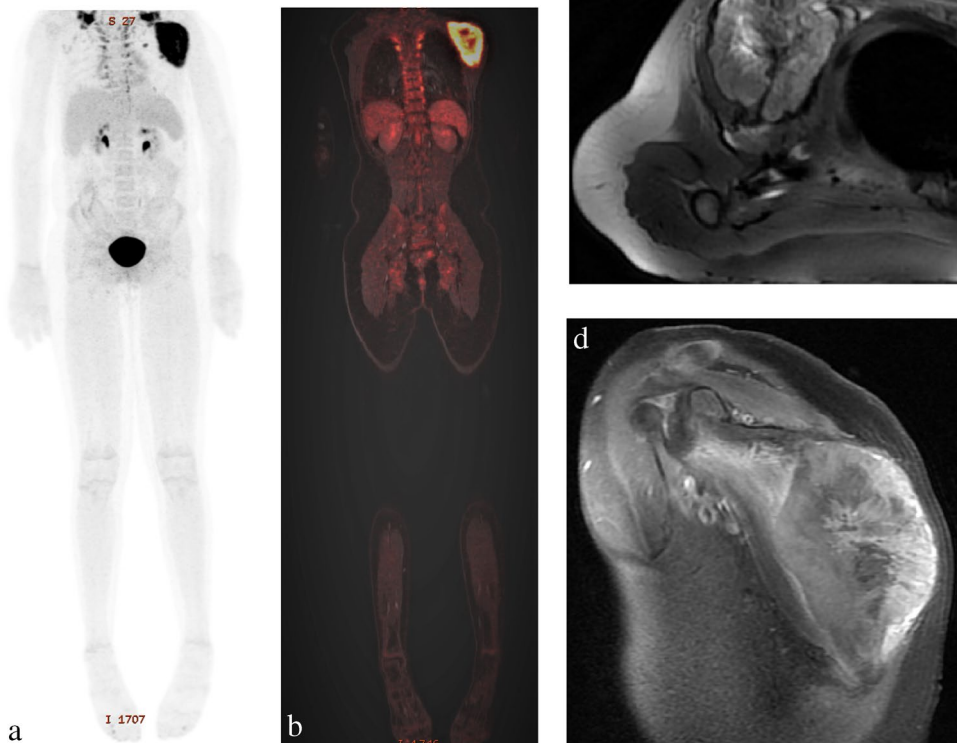
Ewing sarcomas present as T1-hypointense, T2-hyperintense, often heterogenous, contrast enhancing bone tumors that infiltrate into the surrounding soft tissues (Fig. 5a–d). A comprehensive MRI exam includes one T1-SE sequence that covers the entire affected bone from joint to joint, followed by a small-FOV local scan to evaluate anatomical details. The primary tumor is measured in three dimensions and the tumor volume is calculated according to the formula for a prolate ellipsoid: volume in $\text{mm}^3 = \pi/6 \cdot (\text{d}_1 \cdot \text{d}_2 \cdot \text{d}_3) = (\text{AP} \times \text{transverse} \times \text{longitudinal}) \times 0.5$. These

tumors demonstrate restricted diffusion on MRI and are hypermetabolic on ^{18}F -FDG-PET/MRI scans, with the degree of ^{18}F -FDG uptake correlating with tumor stage and patient survival [58]. In a heterogenous tumor, ^{18}F -FDG-PET can help guide biopsy region of the highest metabolic activity [59]. A pre-therapy SUV threshold of approximately 12 or higher has correlated to poor therapy response in previous studies [60, 61].

In patients with Ewing sarcomas, ^{18}F -FDG-PET is used for detection of metastases and integrated ^{18}F -FDG-PET/MR can provide efficient local and whole-body staging in one session [62]. ^{18}F -FDG-PET is considered more sensitive than conventional bone scintigraphy for detecting osseous lesions (88% for ^{18}F -FDG-PET versus 37% for bone scintigraphy) [63]. Ewing sarcomas can have a specific affinity for the pancreas and, therefore, the pancreas should always be carefully evaluated for metastases. ^{18}F -FDG-PET can detect disease progression earlier than relying on CT or MRI alone [59, 64].

Conventional therapy for Ewing sarcoma includes initial chemotherapy followed by radiation and/or surgery. Adjuvant chemotherapy is also included to reduce the risk of recurrence. On MRI, chemotherapy response is measured based on three-dimensional measurements of the primary tumor and up to five index metastases with a diameter of more than 1 cm. Most Ewing sarcomas demonstrate significant decrease in size and increased ADC values in response

Fig. 5 Left scapula Ewing sarcoma in a 15-year-old male presenting with left scapular mass. **a** PET/MR whole-body coronal MIP and **b** PET/MR whole-body coronal T1-weighted fat-suppressed fused images showing an intensely ^{18}F -FDG-avid mass centered in the left scapula (SUV max 7.1) with central necrosis. Note that we scanned the patients' head in the supine position and then scanned the whole body in the prone position due to pain in the left scapula. **c** Prone axial T2-weighted fat-suppressed MR image showing a lobulated, inhomogenous, mostly hyperintense mass in the left scapula with large associated soft tissue component and surrounding edema in the supraspinatus, infraspinatus, and subscapularis muscles. **d** Sagittal T1-weighted fat-saturated postcontrast MR image of the left scapula showing contrast-enhancement of the mass and infiltration of the surrounding rotator cuff musculature



to chemotherapy, likely due to increased proton diffusion related to decreased tumor bulk [65]. ^{18}F -FDG-PET can add information: reduced ^{18}F -FDG uptake of greater than 30% after chemotherapy is a strong indicator of treatment response [66]. A difference in pre- and post-treatment SUVs of 0.5 or less correlated to poor therapy response [67].

Bone lymphoma

Bone lymphoma can rarely occur due to secondary involvement of the bone marrow in patients with classical Hodgkin lymphoma or non-Hodgkin lymphoma. Primary bone lymphomas, which are defined as single or multiple osseous lesions without associated nodal or visceral involvement, are rare, representing < 2% of lymphomas in adults and 3–7% of all primary bone tumors [68]. The major subtypes are diffuse large B cell lymphoma and lymphoblastic lymphoma. The 5-year survival rate is > 80% [69]. Bone lymphomas present as T1-hypointense bone marrow lesions with markedly restricted diffusion [65]. The T2-signal is often lower compared to other malignant tumors, such as sarcomas [70]. The cortex of the bone is typically intact and shows no or minimal signs of destruction because the tumor spreads through the Haversian canals. ^{18}F -FDG-PET has up to a 100% positive predictive value in diagnosing active disease and can help assess for extraskeletal lesions which would exclude the diagnosis of primary bone lymphoma [71, 72].

Patients with lymphoma of the bone are treated with chemotherapy and often show impressive response on interim scans, classified according to the Lugano criteria [73]. The ^{18}F -FDG tumor signal is expected to be below that of mediastinal blood pool on interim scans and below that of the liver on end-of-therapy scans.

Bone and bone marrow metastases

The most common primary tumors for bone and bone marrow metastases in children are neuroblastoma, soft tissue sarcomas, and osseous sarcomas [74]. These malignancies all metastasize hematogenously and therefore favor the highly vascular red marrow. Often, ^{131}I -meta-iodo benzylguanine (^{131}I -MIBG) is the conventional imaging modality for evaluating neuroblastoma, as it shows a sensitivity of about 90% and a specificity of nearly 100% for imaging neuroblastoma [75]. However, ^{18}F -FDG-PET can add information in the case of ^{131}I -MIBG non-avid tumors, as FDG may accumulate in the < 20% of neuroblastomas that do not concentrate radioactive tracers particular to the sympathetic nervous system and FDG uptake does not depend on type 1 catecholamine uptake [76, 77]. Since MRI is used for local

staging of neuroblastoma, adding ^{18}F -FDG-PET can provide “one stop” local and whole-body staging, thereby decreasing radiation exposure and duplicate anesthesia [12]. An interesting evolution are ^{131}I -MIBG-equivalent PET tracers, such as ^{18}F -meta-fluorobenzylguanidine.

Langerhans cell histiocytosis

Langerhans cell histiocytosis (LCH) is due to a proliferation of mononuclear cells, or histiocytes, that typically manifest in young children and can be associated with BRAF V600E mutation [78]. LCH can manifest in a single or multiple systems including the bone marrow/bone, lymph nodes, skin, visceral organs, and brain—especially the pituitary gland with clinical signs of diabetes insipidus [79].

^{18}F -FDG-PET/CT has been shown to be superior to the conventional imaging methods (including bone surveys, MR, CT, or bone scans) for identifying active lesions, treatment response, and identifying disease stage [80]. Since patients with multifocal LCH typically are very young and need multiple follow-up studies, replacing CT with MR for co-registration of ^{18}F -FDG-PET data can substantially reduce their cumulative radiation exposure [12]. In the proliferation phase, LCH lesions appear T2-hyperintense and demonstrate restricted diffusion, positive MR contrast enhancement, and marked ^{18}F -FDG uptake (Fig. 6a–d) [5, 81]. A successfully treated LCH lesions appears T2-iso- or hypointense and demonstrates no or minimal restricted diffusion, less MR contrast enhancement, decreased signal intensity on STIR, and less ^{18}F -FDG uptake [82, 83].

Summary

In summary, the use of ^{18}F -FDG-PET/MRI has many utilities in diagnosing and evaluating bone tumors, both primary and metastatic. The combination of functional ^{18}F -FDG-PET imaging with the lack of non-ionizing radiation of MRI is ideal in a pediatric population that likely requires frequent scanning. The use of MRI also affords stronger evaluation of soft tissues compared to CT.

There are, however, limitations associated with ^{18}F -FDG-PET/MRI. The acquisition of a whole-body scan and a local tumor scan in one session is time-consuming, even when streamlined protocols are applied. New technical developments are needed that substantially accelerate image acquisition times. Additionally, evaluation of the lungs, which is frequently required with bone tumors, requires the addition of chest CT in addition to ^{18}F -FDG-PET/MRI. Finally, there are disease processes that can lead to false positives such as osteomyelitis and trauma, although the experienced radiologist can differentiate most benign and malignant lesions in children based on characteristic imaging findings.

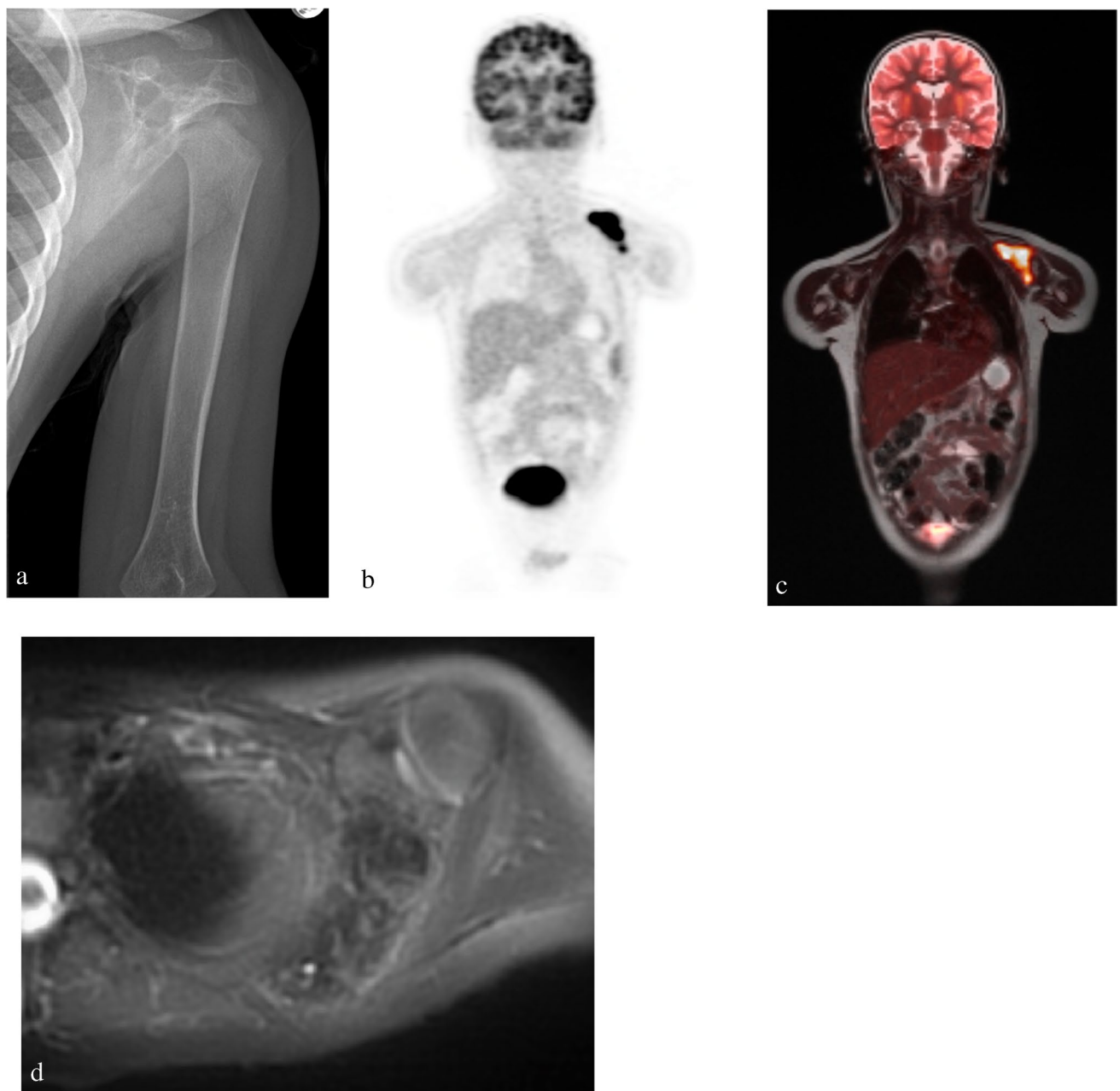


Fig. 6 Langerhans cell histiocytosis of the left scapula discovered on a skeletal survey in a 2-year-old male presenting with right facial nerve palsy and a mass on the right forehead. **a** Frontal radiograph of the left scapula showing an expansile, lytic lesion involving the acromion, glenoid, and scapular body with a normal left humerus.

b ^{18}F -FDG PET/MR whole-body coronal MIP, **c** PET/MR: coronal T2-weighted MRI scan fused with ^{18}F -FDG PET scan, and **d** axial T2-weighted fat-suppressed MR images showing a highly ^{18}F -FDG-avid (SUV max 15.8), T2 hypointense lesion involving the left scapular acromion and body

Future outlook

In the future, improved sequences of the lungs may likely eliminate the need for an additional chest CT, which still remains a necessity given the limited resolution of ^{18}F -FDG-PET/MRI for evaluation of lung nodules. In addition, the development of new radiotracers can further expand the use of ^{18}F -FDG-PET/MRI. Some potential pediatric radiotracers

in development include [11C]-(*R*)-(2-chlorophenyl)-N-methyl-N-(1-methylpropyl)-3-isoquinoline-carboxamide [(11) C-(*R*)-PK11195] to image activated macrophages and 6-(3-(*18*F)fluoropropyl)-3-(2-(azepan-1-ethyl)benzo(d)thiazol-2 (**18**F-FTC-146) to image sigma 1 receptors as early markers of pain. Amino acid radiotracers such as ^{18}F -meta-fluorobenzylguanidine and ^{18}F -DOPA are new radiotracers being used off label to evaluate neuroendocrine malignancies

and brain tumors. Similarly, ⁶⁸Ga-DOTATATE has been increasingly used off label for imaging neuroendocrine tumors in the pediatric population.

Key points

1. Integrated ¹⁸F-FDG-PET/MRI is valuable for imaging bone lesions in the pediatric population, assessing the primary tumor and whole-body metastases in a single session.
2. Important reporting considerations for radiologists reading ¹⁸F-FDG-PET/MRI scans include describing tumor size, presence or absence of metastatic disease and location of metastases, and changes in size of index lesions for treatment monitoring.
3. Soft tissue components of conventional osteosarcoma are often T2-hyperintense and ¹⁸F-FDG avid on PET while the bone forming components are often T2-hypointense and have low ¹⁸F-FDG avidity. Descriptions of the extent of intra- and extra-osseous soft tissue, neurovascular bundle involvement, presence of intra-articular extension and tumor thrombus are important as these can have implications on treatment planning.
4. In [Ewing sarcoma](#), ¹⁸F-FDG-PET/MRI can help guide biopsy planning towards tumor areas that exhibit the highest metabolic activity. ¹⁸F-FDG PET/MRI can help gauge tumor chemotherapy response based on reduced ¹⁸F-FDG uptake of greater than 30%.

Highlights

- Integrated ¹⁸F-FDG-PET/MRI in the pediatric population provides simultaneous primary tumor evaluation and staging without ionizing radiation, making it a valuable alternative to traditional multistep ¹⁸F-FDG-PET/CT and local MRI.
- The imaging technique we use at our institution involves a 60-min exam, which includes a whole-body and local tumor scan. ¹⁸F-FDG-PET scans can be fused with sequentially acquired Gd-chelate enhanced MRI scans or with simultaneously acquired MRI scans at 1–2 h after intravenous administration of iron oxide nanoparticles.
- Radiology reports for ¹⁸F-FDG-PET/MRI scans should include primary tumor location and three-dimensional tumor size, as well as presence or absence of vascular involvement, tumor thrombus, joint involvement, pathologic fracture, and metastatic disease.

Funding This study was in part supported by a grant from the National Cancer Institute (NCII, R01CA269231) and a grant from the Andrew McDonough B + Foundation.

Declarations

Conflict of interest The authors declare no competing interests.

References

1. Hardin AP, Hackell JM, Simon GR, Boudreau ADA, Baker CN, Barden GA, et al. Age limit of pediatrics. *Pediatrics*. 2017;140:3–5.
2. Schäfer JF, Gatidis S, Schmidt H, Gückel B, Bezrukov I, Pfannenberg CA, et al. Simultaneous whole-body PET/MR imaging in comparison to PET/CT in pediatric oncology: initial results. *Radiology*. Radiol Soc N Am Inc. 2014;273:220–31.
3. Lyons K, Seghers V, Sorensen JIL, Zhang W, Paldino MJ, Krishnamurthy R, et al. Comparison of standardized uptake values in normal structures between PET/CT and PET/MRI in a tertiary pediatric hospital: a prospective study. *AJR Am J Roentgenol*. 2015;205:1094–101.
4. Buchbender C, Heusner TA, Lauenstein TC, Bockisch A, Antoch G. Oncologic PET/MRI, part 2: bone tumors, soft-tissue tumors, melanoma, and lymphoma. *J Nucl Med*. 2012;53:1244–52.
5. Rashidi A, Baratto L, Theruvath AJ, Greene EB, Hawk KE, Lu R, et al. Diagnostic accuracy of 2-[¹⁸F]FDG-PET and whole-body DW-MRI for the detection of bone marrow metastases in children and young adults. *Eur Radiol*. 2022;32(7):4967–4979.
6. Jeon M, Halbert M, Stephen ZR, Zhang M. Iron oxide nanoparticles as T1 contrast agents for magnetic resonance imaging: fundamentals, challenges, applications, and perspectives. *Adv Mater*. 2021;33:1–18.
7. Avasthi A, Caro C, Pozo-Torres E, Leal MP, García-Martín ML. Magnetic nanoparticles as MRI contrast agents. *Top Curr Chem*. 2020;378:40.
8. Stephen ZR, Kievit FM, Zhang M. Magnetite nanoparticles for medical MR imaging. *Mater Today*. 2011;14:330–8.
9. Yoo HJ, Lee JS, Lee JM. Integrated whole body MR/PET: where are we? *Korean J Radiol*. 2015;16:32.
10. Pareek A, Muehe AM, Theruvath AJ, Gulaka PK, Spunt SL, Daldrup-Link HE. Whole-body PET/MRI of pediatric patients: the details that matter. *J Vis Exp*. 2017;130:57128.
11. Ramalho M, AlObaidy M, Catalano OA, Guimaraes AR, Salvatore M, Semelk RC. MR-PET of the body: early experience and insights. *Eur J Radiol Open*. 2014;1:28–39.
12. States LJ, Reid JR. Whole-body PET/MRI applications in pediatric oncology. *AJR Am J Roentgenol*. 2020;215:713–25.
13. Ehman EC, Johnson GB, Villanueva-Meyer JE, Cha S, Leynes AP, Larson PEZ, et al. PET/MRI: where might it replace PET/CT? *J Magn Reson Imaging*. 2017;46:1247–62.
14. Mannheim JG, Schmid AM, Schwenck J, Katiyar P, Herfert K, Pichler BJ, et al. PET/MRI hybrid systems. *Semin Nucl Med*. 2018;48:332–47.
15. Geiger J, Zeimpekis KG, Jung A, Moeller A, Kellenberger CJ. Clinical application of ultrashort echo-time MRI for lung pathologies in children. *Clin Radiol*. 2021;76:708.e9–708.e17.
16. Aghighi M, Boe J, Rosenberg J, Von ER, Gawande RS, Petit P, et al. Three-dimensional radiologic assessment of chemotherapy response in Ewing sarcoma can be used to predict clinical outcome. *Radiology*. 2016;280:905–15.
17. Oprea-Lager DE, Cysouw MCF, Boellaard R, Deroose CM, de Geus-Oei LF, Lopci E, et al. Bone metastases are measurable: the role of whole-body MRI and positron emission tomography. *Front Oncol*. 2021;11:4948.

18. Nishino M, Jagannathan JP, Ramaiya NH, VanDenAbbeele AD. Revised RECIST guideline version 1.1: what oncologists want to know and what radiologists need to know. *AJR Am J Roentgenol.* 2010;195:281–9.
19. Mirabello L, Troisi RJ, Savage SA. International osteosarcoma incidence patterns in children and adolescents, middle ages and elderly persons. *Int J cancer.* 2009;125:229–34.
20. Brenner W, Bohuslavizki KH, Eary JF. PET imaging of osteosarcoma. *J Nucl Med.* 2003;44:930–42.
21. Murphey MD, Robbin MR, McRae GA, Flemming DJ, Temple HT, Kransdorf MJ. The many faces of osteosarcoma. *Radiographics.* 1997;17:1205–31.
22. Siegel RL, Miller KD, Fuchs HE, Jemal A. Cancer Statistics, 2021. *CA Cancer J Clin.* 2021;71:7–33.
23. Bielack SS, Kempf-Bielack B, Delling G, Exner GU, Flege S, Helmke K, et al. Prognostic factors in high-grade osteosarcoma of the extremities or trunk: an analysis of 1,702 patients treated on Neoadjuvant Cooperative Osteosarcoma Study Group Protocols. *J Clin Oncol.* 2002;20:776–90.
24. Haveman LM, Ranft A, vdBerg H, Smets A, Kruseova J, Ladenstein R, et al. The relation of radiological tumor volume response to histological response and outcome in patients with localized Ewing Sarcoma. *Cancer Med.* 2019;8:1086–94.
25. Yarmish G, Klein MJ, Landa J, Lefkowitz RA, Hwang S. Imaging characteristics of primary osteosarcoma: nonconventional subtypes. *Radiographics.* 2010;30:1653–72.
26. Yoshida A. Osteosarcoma: old and new challenges. *Surg Pathol Clin.* 2021;14:567–83.
27. Daldrup-Link HE. How PET/MR can add value for children with cancer. *Curr Radiol Rep.* 2017;5.
28. Yedururi S, Morani AC, Gladish GW, Vallabhaneni S, Anderson PM, Hughes D, et al. Cardiovascular involvement by osteosarcoma: an analysis of 20 patients. *Pediatr Radiol.* 2016;46:21–33.
29. Murphey MD, Wan Jaovisidha S, Temple HT, Gannon FH, Jelinek JS, Malawer MM. Telangiectatic osteosarcoma: radiologic-pathologic comparison. *Radiology.* 2003;229:545–53.
30. Discepola F, Powell TI, Nahal A. Telangiectatic osteosarcoma: radiologic and pathologic findings. *Radiographics.* 2009;29:380–3.
31. Murphey MD, Jelinek JS, Temple HT, Flemming DJ, Gannon FH. Imaging of periosteal osteosarcoma: radiologic-pathologic comparison. *Radiology.* 2004;233:129–38.
32. Harper K, Sathiadoss P, Saifuddin A, Sheikh A. A review of imaging of surface sarcomas of bone. *Skeletal Radiol.* 2021;50:9–28.
33. Kumar VS, Barwar N, Khan SA. Surface osteosarcomas: diagnosis, treatment and outcome. *Indian J Orthop.* 2014;48:255–61.
34. Ayerza MA, Farfalli GL, Aponte-Tinao L, Luis MD. Does increased rate of limb-sparing surgery affect survival in osteosarcoma? *Clin Orthop Relat Res.* 2010;468:2854–9.
35. Quan GMY, Slavin JL, Schlicht SM, Smith PJ, Powell GJ, Choong PFM. Osteosarcoma near joints: assessment and implications. *J Surg Oncol.* 2005;91:159–66.
36. Schima W, Amann G, Stiglbauer R, Windhager R, Kramer J, Nicolakis M, et al. Preoperative staging of osteosarcoma: efficacy of MR imaging in detecting joint involvement. *AJR Am J Roentgenol.* 1994;163:1171–5.
37. Eaton BR, Schwarz R, Vatner R, Yeh B, Claude L, Indelicato DJ, et al. 2021 Osteosarcoma. *Pediatr Blood Cancer.* 68.
38. Navalkele P, Jones SM, Jones JK, Salazar JD, Toy PC, Iyer RV, et al. Osteosarcoma tumor thrombus: a case report with a review of the literature. *Texas Hear Inst J.* 2013;40:75–8.
39. Liang H, Guo W, Yang R, Tang X, Yan T, Ji T, et al. Radiological characteristics and predisposing factors of venous tumor thrombus in pelvic osteosarcoma: a mono-institutional retrospective study of 115 cases. *Wiley Online Libr.* 2018;7:4903–13.
40. Nguyen JC, Baghdadi S, Pogoriler J, Guariento A, Rajapakse CS, Arkader A. 2022 Pediatric osteosarcoma: correlation of imaging findings with histopathologic features, treatment, and outcome. *Radiographics.* 210171.
41. Muehe AM, Theruvath AJ, Lai L, Aghighi M, Quon A, Holdsworth SJ, et al. How to provide gadolinium-free PET/MR cancer staging of children and young adults in less than 1 h: the Stanford approach. *Mol imaging Biol.* 2018;20:324–35.
42. Kara PO, Sezer Y, Koc ZP, Yilmaz EB, Citak EC, Ozcan P, et al. 2018 Role of FDG PET-CT in distinction of benign thrombus and tumor thrombus in oncological patients. *Biomed J Sci & Tech Res.* 2.
43. Enneking WF, Kagan A. “Skip” metastases in osteosarcoma. *Cancer.* 1975;36:2192–205.
44. Jiya TU, Wuismans PIJM. Long-term follow-up of 15 patients with non-metastatic Ewing’s sarcoma and a skip lesion. *Acta Orthop.* 2005;76:899–903.
45. Sajadi KR, Heck RK, Neel MD, Rao BN, Daw N, Rodriguez-Galindo C, et al. The incidence and prognosis of osteosarcoma skip metastases. *Clin Orthop Relat Res.* 2004;426:92–6.
46. Kager L, Zoubek A, Kastner U, Kempf-Bielack B, Potratz J, Kotz R, et al. Skip metastases in osteosarcoma: experience of the Cooperative Osteosarcoma Study Group. *J Clin Oncol.* 2006;24:1535–41.
47. San-Julian M, Diaz-de-Rada P, Noain E, Sierrasesumaga L. Bone metastases from osteosarcoma. *Int Orthop.* 2003;27:117–20.
48. Quartuccio N, Fox J, Kuk D, Wexler LH, Baldari S, Cistaro A, et al. Pediatric bone sarcoma: diagnostic performance of ¹⁸F-FDG PET/CT versus conventional imaging for initial staging and follow-up. *AJR Am J Roentgenol.* 2015;204:153–60.
49. Faisham WI, Mat Saad AZ, Alsaigh LN, Nor Azman MZ, Kamarul Imran M, Biswal BM, et al. Prognostic factors and survival rate of osteosarcoma: a single-institution study. *Asia Pac J Clin Oncol.* 2017;13:e104–10.
50. Bajpai J, Gamnagatti S, Kumar R, Sreenivas V, Sharma MC, Khan SA, et al. Role of MRI in osteosarcoma for evaluation and prediction of chemotherapy response: correlation with histological necrosis. *Pediatr Radiol.* 2011;41:441–50.
51. Hanafy E, Al Jabri A, Gadelkarim G, Dasaq A, Nazim F, Al PM. Tumor histopathological response to neoadjuvant chemotherapy in childhood solid malignancies: is it still impressive? *J Investig Med.* 2018;66:289–97.
52. Davis JC, Daw NC, Navid F, Billups CA, Wu J, Bahrami A, et al. 18 F-FDG uptake during early adjuvant chemotherapy predicts histologic response in pediatric and young adult patients with osteosarcoma. *J Nucl Med.* 2018;59:25–30.
53. Dou X, Yan H, Wang R. Treatment of an Askin tumor: a case report and review of the literature. *Oncol Lett.* 2013;6:985–9.
54. Grünewald TGP, Cidre-Aranaz F, Surdez D, Tomazou EM, De Álava E, Kovar H, et al. 2018 Ewing sarcoma. *Nat Rev Dis Prim.* 4.
55. Choi JH, Ro JY. The 2020 WHO classification of tumors of soft tissue: selected changes and new entities. *Adv Anat Pathol.* 2021;28:44–58.
56. Gaspar N, Hawkins DS, Dirksen U, Lewis II, Ferrari S, Le Deley MC, et al. Ewing sarcoma: current management and future approaches through collaboration. *J Clin Oncol.* 2015;33:3036–46.
57. Rodríguez-Galindo C, Navid F, Liu T, Billups CA, Rao BN, Krasin MJ. Prognostic factors for local and distant control in Ewing sarcoma family of tumors. *Ann Oncol.* 2008;19:814–20.
58. Guimaraes JB, Rigo L, Lewin F, Emerick A. The importance of PET/CT in the evaluation of patients with Ewing tumors. *Radiol Bras.* 2015;48:175–80.
59. Bestic JM, Peterson JJ, Bancroft LW. Pediatric FDG PET/CT: Physiologic uptake, normal variants, and benign conditions. *Radiographics.* 2009;29:1487–500.

60. Salem U, Amini B, Chuang HH, Daw NC, Wei W, Haygood TM, et al. 18 F-FDG PET/CT as an indicator of survival in Ewing sarcoma of bone. *J Cancer*. 2017;8:2892–8.
61. Jamet B, Carlier T, Campion L, Bompas E, Girault S, Borrelly F, et al. Initial FDG-PET/CT predicts survival in adults Ewing sarcoma family of tumors. *Oncotarget*. 2017;8:77050–60.
62. Muehe AM, Siedek F, Theruvath AJ, Seekins J, Spunt SL, Pribnow A, et al. Differentiation of benign and malignant lymph nodes in pediatric patients on ferumoxytol-enhanced PET/MRI. *Theranostics*. 2020;10:3612–21.
63. Völker T, Denecke T, Steffen I, Misch D, Schönberger S, Plotkin M, et al. Positron emission tomography for staging of pediatric sarcoma patients: results of a prospective multicenter trial. *J Clin Oncol*. 2007;25:5435–41.
64. Javery O, Krajewski K, O'Regan K, Kis B, Giardino A, Jagannathan J, et al. 2011 A to Z of extraskeletal Ewing sarcoma family of tumors in adults: imaging features of primary disease, metastatic patterns, and treatment responses. *AJR Am J Roentgenol*. 197.
65. Theruvath AJ, Siedek F, Muehe AM, Garcia-Diaz J, Kirchner J, Martin O, et al. Therapy response assessment of pediatric tumors with whole-body diffusion-weighted MRI and FDG PET/MRI. *Radiology*. 2020;296:143–51.
66. Franzius C, Sciuik J, Schmidt CB, Jürgens H, Schober O. Evaluation of chemotherapy response in primary bone tumors with F-18 FDG positron emission tomography compared with histologically assessed tumor necrosis. *Clin Nucl Med*. 2000;25:874–81.
67. Hawkins DS, Schuetze SM, Butrynski JE, Rajendran JG, Vernon CB, Conrad EU, et al. [18F]Fluorodeoxyglucose positron emission tomography predicts outcome for Ewing sarcoma family of tumors. *J Clin Oncol*. 2005;23:8828–34.
68. Bindal P, Desai A, Delasos L, Mulay S, Vredenburgh J. Primary bone lymphoma: a case series and review of literature. *Case Rep Hematol*. 2020;2020:1–6.
69. Milks KS, McLean TW, Anthony EY. Imaging of primary pediatric lymphoma of bone. *Pediatr Radiol*. 2016;46:1150–7.
70. Zhou HY, Gao F, Bu B, Fu Z, Sun XJ, Huang CS, et al. Primary bone lymphoma: a case report and review of the literature. *Oncol Lett*. 2014;8:1551–6.
71. Kaddu-Mulindwa D, Altmann B, Held G, Angel S, Stilgenbauer S, Thurner L, et al. FDG PET/CT to detect bone marrow involvement in the initial staging of patients with aggressive non-Hodgkin lymphoma: results from the prospective, multicenter PETAL and OPTIMAL>60 trials. *Eur J Nucl Med Mol Imaging*. 2021;48:3550–9.
72. Liu Y. The role of 18F-FDG PET/CT in staging and restaging primary bone lymphoma. *Nucl Med Commun*. 2017;38:319–24.
73. Friedman DL, Chen L, Wolden S, Buxton A, McCarten K, FitzGerald TJ, et al. Dose-intensive response-based chemotherapy and radiation therapy for children and adolescents with newly diagnosed intermediate-risk hodgkin lymphoma: a report from the Children's Oncology Group Study AHOD0031. *J Clin Oncol*. 2014;32:3651–8.
74. Chan BY, Gill KG, Rebsamen SL, Nguyen JC. MR imaging of pediatric bone marrow. *Radiographics*. 2016;36:1911–30.
75. Sharp SE, Shulkin BL, Gelfand MJ, Salisbury S, Furman WL. 123 I-MIBG scintigraphy and 18 F-FDG PET in neuroblastoma. *J Nucl Med*. 2009;50:1237–43.
76. Atkin KL, Ditchfield MR. The role of whole-body MRI in pediatric oncology. *J Pediatr Hematol Oncol*. 2014;36:342–52.
77. Shulkin BL, Hutchinson RJ, Castle VP, Yanik GA, Shapiro B, Sisson JC. Neuroblastoma: Positron emission tomography with 2-[fluorine-18]-fluoro-2-deoxy-D-glucose compared with meta-iodobenzylguanidine scintigraphy. *Radiology*. 1996;199:743–50.
78. Thacker NH, Abla O. Pediatric Langerhans cell histiocytosis: state of the science and future directions. *Clin Adv Hematol Oncol*. 2019;17:122–31.
79. Makras P, Samara C, Antoniou M, Zetos A, Papadogias D, Nikolaopoulou Z, et al. Evolving radiological features of hypothalamo-pituitary lesions in adult patients with Langerhans cell histiocytosis (LCH). *Neuroradiology*. 2006;48:37–44.
80. Sher AC, Orth R, McClain K, Allen C, Hayatghaibi S, Seghers V. PET/MR in the assessment of pediatric histiocytoses: a comparison to PET/CT. *Clin Nucl Med*. 2017;42:582–8.
81. Váradi Z, Bánusz R, Csomor J, Kálly K, Varga E, Kertész G, et al. Effective BRAF inhibitor vemurafenib therapy in a 2-year-old patient with sequentially diagnosed Langerhans cell histiocytosis and Erdheim-Chester disease. *Onco Targets Ther*. 2017;10:521–6.
82. Guimarães MD, Noschang J, Teixeira SR, Santos MK, Lederman HM, Tostes V, et al. 2017 Whole-body MRI in pediatric patients with cancer. *Cancer Imaging*. 17.
83. Phillips M, Allen C, Gerson P, McClain K. Comparison of FDG-PET scans to conventional radiography and bone scans in management of Langerhans cell histiocytosis. *Pediatr Blood Cancer*. 2009;52:97–101.

Publisher's Note Springer Nature remains neutral with regard to jurisdictional claims in published maps and institutional affiliations.